Article

Synthesis and preliminary in vivo evaluation of well-dispersed biomimetic nanocrystalline apatites labeled with positron emission tomographic imaging agents

Benedikt Sandhöfer, Marian Meckel, José Manuel Delgado-López, Tatiana Patricio, Anna Tampieri, Frank Roesch, and Michele Iafisco

ACS Appl. Mater. Interfaces, **Just Accepted Manuscript** • DOI: 10.1021/acsami.5b02624 • Publication Date (Web): 27 Apr 2015

Synthesis and preliminary *in vivo* evaluation of well-dispersed biomimetic nanocrystalline apatites labeled with positron emission tomographic imaging agents

Benedikt Sandhöfer[1], Marian Meckel[1], José Manuel Delgado-López[2], Tatiana Patrício[3], Anna Tampieri[3], Frank Rösch[1,] and Michele Iafisco[3,*]*

[1]Institute of Nuclear Chemistry, Johannes Gutenberg-University, Fritz-Strassmann-Weg 2, 55128, Mainz, Germany.

[2]Instituto Andaluz de Ciencias de la Tierra (IACT), (CSIC-UGR), Laboratorio de Estudios Cristalográficos, Av. Las Palmeras 4, 18100 Armilla, Spain.

[3]Institute of Science and Technology for Ceramics (ISTEC), National Research Council (CNR), Via Granarolo 64, 48018 Faenza, Italy.

KEYWORDS: nanomedicine, calcium phosphates, drug delivery, positron emission tomography, nanoparticles

ABSTRACT: In the last years, biomimetic synthetic apatite nanoparticles (AP-NPs), having chemical similarity with the mineral phase of bone, have attracted a great interest in nanomedicine as potential drug carriers. To evaluate the therapeutic perspectives of AP-NPs through the mechanisms of action and organs they interact with, the non-invasive monitoring of their *in vivo* behavior is of paramount importance. To this aim, here the feasibility to radiolabel AP-NPs ("naked" and surface-modified with citrate to reduce their aggregation) with two positron emission tomographic (PET) imaging agents ([^{18}F]NaF and ^{68}Ga-NO2AP^{BP}) was investigated. [^{18}F]NaF was used for the direct incorporation of the radioisotope into the crystal lattice, while the labeling by surface functionalization was accomplished by using ^{68}Ga-NO2AP^{BP} (a new radio-metal chelating agent). The labeling with both tracers resulted fast, straightforward and reproducible. AP-NPs demonstrated excellent ability to bind relevant quantities of both radiotracers and good *in vitro* stability in clinically relevant media after the labeling. *In vivo* PET studies in healthy Wistar rats established that the radiolabeled AP-NPs gave significant PET signals and they were stable over the investigated time (90 min) since any tracer desorption was detected. These preliminary *in vivo* studies furthermore showed a clear ability of citrated versus "naked" AP-NPs to accumulate in different organs. Interestingly, contrary to "naked" AP-NPs, citrated ones, which unveiled higher colloidal stability in aqueous suspensions, were able to escape the first physiological filter, i.e. the lungs, being then accumulated in the liver and, in less extent, in the spleen. The results of this work, along with the fact that AP-NPs can be also functionalized with targeting ligands, therapeutic agents and also with metals for a combination of different imaging modalities, make AP-NPs very encouraging materials for further investigations as theranostic agents in nanomedicine.

1. INTRODUCTION

The most interesting aspect of using nanoparticles (NPs) in medicine is related to their ability to be specifically localized (or targeted) to the site of disease in order to reduce or even eliminate undesired side effects.[1-2] Different types of NPs, produced from either soft (organic and polymeric) or hard (inorganic) materials, have been evaluated as drug vehicles and some of them have been approved for clinical use.[3-4] Nevertheless, the clinical translation of NPs as drug carriers was hindered by several concerns regarding to their toxicity and biodegradability.[5]

Among the currently studied NPs, the so-called "biomimetic" synthetic apatite (AP) nanocrystals have attracted a great interest in nanomedicine in the last years.[6-8] Usually, AP-based materials are used for bone repair applications due to their well-known properties such as osteoinductivity, bioactivity and biodegradability.[9-10] However, synthetic AP-NPs prepared in close to physiological conditions can exhibit high similarity (in terms of chemical composition, crystal structure and morphology) with the mineral phase of bone. This feature can be extremely useful in nanomedicine to overcome the presently limitations of NPs, since biomimetic AP-NPs can be recognized by the organism as a sort of endogenous material. Moreover, AP-NPs present other numerous interesting properties such as good biodegradability, null toxicity, low production costs and pH-dependent dissolution.[9] This latter property is thought to be useful for the selective release of drug after cellular uptake, since lysosomes exhibit a slightly acidic pH.[6, 9, 11] AP-NPs are also well known for their ability to bind a wide variety of molecules due to their large surface area-to-volume ratio, nano-porosity and presence of available surface ionic sites.[6, 9]

Although numerous studies about the functionalization of AP-NPs with therapeutic agents (such as chemotherapeutic drugs, antibiotic, growth factors, proteins, antibodies, RNA, DNA, etc.)[6, 12-15] and about *in vitro* assays with a high number of different cell lines are well reported,[16-

[19] works about the *in vivo* biodistribution and organ accumulation of AP-NPs are lacking with the exception of a few reports.[20-24] The non-invasive monitoring of *in vivo* AP-NPs behavior is of paramount importance to assess their general biosafety, to determine their mechanisms of action and the organs they interact with and also to find their optimal nano-architecture for desired usage as drug delivery systems.

To this end, imaging using positron emission tomography (PET) represents an ideal tool for such investigations.[25] The major advantages of PET over other molecular imaging techniques are: i) high sensitivity since it allows detection of very low (picomolar) concentrations of the radiotracers, ii) no limit to tissue penetration in any organ and iii) high spatial and temporal resolution.[26] Therefore, PET imaging using radiolabeled NPs has been recently raising great attention in preclinical research and clinical setting.[27-29] However, the construction of radiolabeled NPs is not trivial and generally speaking, the radiolabeling method should be robust, quick, safe, highly efficient and should produce only minimal change to the original properties of NPs.[28-29] Several key issues need to be taken into account, such as how to choose the appropriate isotopes, what chemical reactions can be used to improve the labeling efficiency and how to achieve the best contrast for PET imaging.[26] Radiolabeling methods can be divided into four categories: (i) complexation reaction of radio-metal ions with chelators via coordination chemistry; (ii) direct bombardment of NPs via hadronic projectiles; (iii) synthesis of NPs using a mixture of radioactive and nonradioactive precursors; (iv) chelator-free post-synthetic radiolabeling.[30-31]

The aim of this work is the radiolabeling of biomimetic AP-NPs with two radiotracers ([^{18}F]NaF and ^{68}Ga-NO2AP^{BP}), the investigation of their chemical-physical properties and their *in vivo* behavior in healthy Wistar rats by preliminary PET imaging. Beside the two different

labeling approaches based on the uptake of [^{18}F]NaF or ^{68}Ga-NO2AP^{BP}, two different kinds of AP-NPs were investigated: "naked" and surface modified with citrate. The strategy to use citrate was aimed at reducing the aggregation of AP-NPs, obtaining well-dispersed NPs in aqueous suspensions. The colloidal stability in aqueous solution is a key feature of NPs when used *in vivo* for preventing agglomeration and possible embolization of capillary vessels.

The chelator-free post-synthesis labeling of AP-NPs was achieved by the direct incorporation of the radioisotope (^{18}F) into the apatitic crystal lattice using [^{18}F]NaF. Indeed, [^{18}F]NaF is a well-established radiotracer for bone PET imaging since fluoride ions can easily enter in AP crystal lattice by ionic exchange with hydroxyl groups.[32] Additionally, [^{18}F]NaF was selected as radiotracer due to the widespread clinical use of [^{18}F]2-deoxy-2-fluoro-D-gluocose (FDG) and because ^{18}F is a widely available isotope daily produced in cyclotrons in most of the major hospitals and distribution centers.[33] In addition, it has excellent physical properties for PET imaging in terms of half-life ($t_{1/2}$) and high-yield low-energy positron.[33]

On the other hand, ^{68}Ga-NO2AP^{BP}, which is a macrocyclic 1,4,7-triazacyclononane-1,4,7-N,N',N''-triacetic acid (NOTA) chelator connected to a bisphosphonate-containing side arm (ESI Fig. S1), was used to evaluate the surface functionalization of AP-NPs with radio-metal ions chelating agents. This complex has been recently prepared by Holub et al.[34] as PET radiotracer for bone imaging. It demonstrated high ability to bind bone AP due to the affinity of its bisphosphonate arm for calcium site, being thus a good candidate to be strongly linked to AP.

The $t_{1/2}$ of ^{18}F and ^{68}Ga are in a similar time scale (110 min and 68 min, respectively) functional for the most PET experiments,[25] especially to gain first insights into the *in vivo* distribution of NPs. Compared to the cyclotron-produced ^{18}F-fluoride, the radio-metal ^{68}Ga can be conveniently obtained from a ^{68}Ge/^{68}Ga-generator system. While the radiolabeling with

$[^{18}F]F^-$ can be achieved in one single step, the labeling with ^{68}Ga needs a previous complexing step with the bifunctional chelator $NO2AP^{BP}$. Indeed this method offers the advantage of using other radionuclides, like ^{44}Sc ($t_{1/2}$=3.9 h) or ^{64}Cu ($t_{1/2}$=12 h), which enable the possibility of long-term PET examination.

This work mainly reflects a tool of medicinal chemistry as it optimizes the structure of the AP-NPs following the rational of experimental correlations between structure (size, surface-modification, etc.) and *in vivo* behavior after injection (PET molecular imaging).

2. EXPERIMENTAL SECTION

2.1. Materials.

Acetylacetone ($CH_3COCH_2COCH_3$, ReagentPlus®), acetone ($(CH_3)_2CO$, capillary GC grade), ammonium hydroxide solution (NH_4OH, ACS reagent, 28.0-30.0% NH_3 basis), calcium acetate hydrate ($(CH_3COO)_2Ca{\cdot}xH_2O$, BioXtra), HEPES sodium salt ($C_8H_{17}N_2NaO_4S$, BioXtra), hydrochloric acid (HCl, ACS reagent, 37 wt% in H_2O), phosphate buffer saline (PBS, 10× concentrate, BioPerformance Certified), phosphoric acid (H_3PO_4, ≥85 wt.% in H_2O), potassium fluoride (KF, ACS reagent), sodium bicarbonate ($NaHCO_3$, BioXtra), sodium chloride (NaCl, BioXtra), sodium citrate tribasic dihydrate ($Na_3(Cit){\cdot}2H_2O$ where Cit=citrate=$C_6H_5O_7$, ACS reagent) and sodium hydroxide (NaOH, ACS reagent) were purchased from Sigma Aldrich. Ultrapure water (0.22 μS, 25 °C, Milli-Q, Millipore) was used in all of the experiments.

2.2. Synthesis of apatite nanoparticles.

Apatite (AP) nanocrystals were synthesized at room temperature dropping a solution of H_3PO_4 (0.21 M) into a solution of $Ca(CH_3COO)_2$ (0.35 M) maintaining the pH at constant value of 10

by addition of NH_4OH. The reaction mixture was kept under stirring at room temperature overnight, then the stirring was suspended and the mixture was left standing for 2 h to allow the deposition of the inorganic phase. This latter was isolated by 10 min of centrifugation at 5000 rpm of the reaction mixture, repeatedly washed with water and suspended in defined amounts of ultrapure water. The concentrations of these suspensions (in terms of mg of AP in 1 ml of water) were established determining the weight of AP in different aliquots after freeze-drying at -60 °C under vacuum (3 mbar) overnight.

Citrated-AP (Cit-AP) nanocrystals were prepared bringing the naked AP suspensions to a concentration of about 10 mg ml^{-1} and adding $Na_3(Cit)$ to obtain a concentration of 67 mM. These suspensions were stirred at room temperature for 2 h, transferred to tubular cellulose membrane (length 10 cm, diameter 22 mm; cut-off 3500 Da) and dialyzed against a large excess of ultrapure water for 24 h to eliminate the unreacted citrate. The evolution of the dialysis efficacy as a function of time was monitored measuring the conductivity of the dialysate solution with a Eutech Instruments CON 2007 conductimeter. The concentrations of NPs suspensions after dialysis were determined as described above.

Part of AP and Cit-AP were freeze-dried at -60 °C under vacuum (3 mbar) overnight for further characterizations.

2.3. Characterization of apatite nanoparticles.

X-ray diffraction (XRD) patterns of the powder samples were recorded with a Bruker D8 Advance diffractometer equipped with a Lynx-eye position sensitive detector using Cu Kα radiation (λ=1.54178 Å) generated at 40 kV and 40 mA. XRD spectra were recorded in the 2θ range from 10 to 60° with a step size (2θ) of 0.02° and a counting time of 0.5 s. The apparent

crystallite sizes along the *c*-axis and along a perpendicular to it were calculated applying the Scherrer's formula[35] using the 2θ=26° and 2θ=39° diffraction peaks, corresponding to the (002) and (310) reflections, respectively.

Transmission electron microscopy (TEM) analyses were performed with a Philips CM 100 instrument operating at 80 kV. The powder samples were ultrasonically dispersed in ultrapure water and few droplets of the slurry were deposited on conventional carbon coated copper micro-grids (400 mesh).

Fourier Transform Infrared (FTIR) spectra were recorded on a Thermo Nicolet 380 FTIR spectrometer. Each powdered sample (about 1 mg) was mixed with about 200 mg of anhydrous KBr and pressed into 7 mm diameter discs. Pure KBr discs were used as background. The infrared spectra were registered from 4000 to 400 cm^{-1} with a resolution of 2 cm^{-1}.

Thermal gravimetric (TGA) analyses of the samples were carried out using a Netzsch STA 449/C Jupiter thermo-microbalance. Sample (about 10 mg) was placed in alumina sample holder and the analyses were performed under a nitrogen flow (100 ml min-1) from room temperature to 1100 °C at a heating rate of 10 °C min^{-1}.

The Ca/P ratio was determined by inductively coupled plasma optical emission spectrometry (ICP-OES) with a Varian Liberty 200 spectrometer. Samples were dissolved in 1 wt% ultrapure nitric acid and the following analytical wavelengths were chosen: Ca 422 nm, P 213 nm.

The specific surface area (SSABET) was determined measuring the nitrogen adsorption at -196 °C according to the BET method with a Micromeritics ASAP 2010 apparatus.

Hydrodynamic size distributions and colloidal stability of the samples were measured at 25 °C by dynamic light scattering (DLS) with a Malvern Zetasizer Nano ZS equipped with a 630 nm laser and a backscattering detector at 173°. NPs suspended in 0.01 M HEPES buffer at pH 7.0

were diluted to a concentration of 1 mg ml^{-1}. Disposable polystyrene cuvettes were used and 3 repetitions of ten runs, 30 s each, were performed for each sample. For the colloidal stability, size and count rate (kcps) were recorded continuously for 100 min.

ζ-potential of the samples was quantified by laser doppler velocimetry measurements through electrophoretic mobility with a Malvern Zetasizer Nano ZS using disposable folded capillary cells at 25 °C. 100 runs were performed in each measurement and 3 measurements for each sample were collected.

2.4. Synthesis of radioactive compounds.

[^{18}F]NaF (150-300 MBq) was prepared by adding a small drop of 0.1 M $NaHCO_3$ to an aqueous solution of ^{18}F-fluoride, prepared from enriched [^{18}O]H_2O by cyclotron irradiation (purchased from DKFZ Heidelberg, Germany).

^{68}Ga-NO2AP^{BP} was prepared by adding 400 µL ^{68}Ga-chloride (200-500 MBq), obtained from a ^{68}Ge/^{68}Ga-generator system (EZAG, Berlin, Germany) in HCl/acetone solution[36] to 15 µg NO2AP^{BP} buffered with 400 µL 0.25 M HEPES solution to pH 4.0. The mixture was heated on a thermo-shaker at 98 °C for 15 min in an open Eppendorf-vessel under moderate shaking. After cooling the radio chemical yield was determined by radio-TLC (Merck silica, solvent: acetylacetone, acetone, HCl) and was found to be over 98 %.[34] For further investigations *in vitro* or *in vivo*, the ^{68}Ga-NO2AP^{BP} solution was neutralized with 1 M NaOH to pH 7.0.

2.5. Labeling of apatite nanoparticles with radiotracers.

2.5.1. Adsorption Kinetics. [^{18}F]NaF (100 µl, 10 MBq) or ^{68}Ga-NO2AP^{BP}, (100 µl containing 1.5 µg of NO2AP^{BP}, 12 MBq) synthesized as reported above, was added to a 1 mg ml^{-1} aqueous

suspension of AP or Cit-AP. The suspension was vortexed for 15 s and incubated at different times for 1, 5 and 10 min. At scheduled times the AP suspensions were centrifuged for 10 min (10000 rpm) at room temperature and the radioactivity in the pellet and the supernatant was measured with an Aktivimeter Isomed 2010 MED (Nuklear-Medizintechnik, Dresden GmbH). Differently, Cit-APs were separated from the supernatant by centrifugal ultrafiltration at 15000 rpm for 10 min using 100 kDa centrifugal filter NanoSep® (Pall Corp. USA) and the radioactivity in the filter and the filtrate was measured using the same instrument described above. The labeling efficiency (reported as percentage of tracer attached to NPs) as a function of time was correlated to the NPs radioactivity and it was calculated using the following equation (1):[37]

$$Labeling\ efficency\ (\%) = \frac{NPs\ Radioactivity}{(NPs\ Radioactivity + Supernatant\ Radioactivity)} \times 100 \qquad (1)$$

2.5.2. Kinetic stability in different media. Kinetic stabilities of the radiolabeled NPs were determined in isotonic saline (0.9 % NaCl, pH 5.5) and PBS (pH 7.4) solutions. [^{18}F]NaF (500 µl, 100 MBq) or 68Ga-NO2APBP (500 µl containing 7.5 µg of NO2APBP, 100 MBq) dissolved in isotonic saline solution were mixed with 500 µl aqueous suspension of AP or Cit-AP-NPs (2 mg ml^{-1}). Each suspension was then added to 1 ml of isotonic saline solution or 2× concentrate PBS. After different periods of incubation ranging from 0 to 120 min, the radioactivity of NPs and supernatant was determined with the aforementioned activimeter. For AP-NP, this was done by centrifugation and re-suspension in the corresponding medium, while samples of Cit-AP NP were prepared for each time point and separated from its supernatant by ultrafiltration. The labeling efficiency as a function of time was correlated to the NPs radioactivity and it was calculated using equation (1).

2.5.3. Adsorption isotherms. 500 µl aqueous suspension of AP or Cit-AP NPs (2 mg ml^{-1}) were added to 500 µl of "cold" NaF ($[^{18}F]F^-$ in trace) or $NO2AP^{BP}$ (^{68}Ga-$NO2AP^{BP}$ in trace) at different concentrations. The stock solutions were prepared by tracing a 1 mg ml^{-1} NaF or $NO2AP^{BP}$ solution with low quantity of $[^{18}F]F^-$ and ^{68}Ga-$NO2AP^{BP}$ (40–60 MBq) having no crucial impact on the NaF or $NO2AP^{BP}$ final amount. To obtain a consistent concentration line, the tracer stock solution was diluted 1:1 with 0.25 M HEPES buffer at pH 7.0 each concentration step (5-8 in total, concentration ranging from 1000 to 3.9 µg ml^{-1}). After adding the tracer to the NPs, the suspension was vortexed for 15 s and allowed to stand for 10 min. Centrifugation (10 min, 10000 rpm) for AP-NPs or centrifugal ultrafiltration for 10 min at 15000 rpm (Nanosep® 100K, Pall Corp. USA) for Cit-AP NPs were used to separate NPs and supernatant. The radioactivity of the pellet or filter and of the supernatant was determined with the same activimeter described above. The amount of tracer attached to the NPs was correlated to the label efficiency (%) evaluated according to equation 1, and it was calculated using the equation (2):

$$Amount\ of\ tracer\ attached\ to\ NPs = \frac{Initial\ amount\ of\ tracer \times Labelling\ efficiency\ (\%)}{100} \qquad (2)$$

2.6. *In vivo* behavior studies.

The *in vivo* experiments with animal models were performed according to the German animal welfare regulations (BGB1. I S. 1206) and to institutional guidelines. The experimental procedure used conforms to the *European Convention for the Protection of Vertebrate Animals used for Experimental and other Scientific Purposes* (86/609/EWG).

0.1 mg (15–22 MBq) of the ^{18}F- or ^{68}Ga-$NO2AP^{BP}$-labeled AP and Cit-AP suspended in 0.5 ml of isotonic saline solution were administrated intravenously (tail vein) in male healthy Wistar

rats, weighting 150-220 g. The rats were put in supine position in a Siemens Focus 120 μPET scanner and anesthetized by inhalation of isoflurane. Dynamic scans were acquired for 90 min and reconstructed using Osem2D. Image processing was done with Pmod software.

2.7. Statistics.

Experiments were performed in triplicates. Data were expressed as mean±standard error. Data obtained from the experiments were compared by a two-tailed t-test. Differences were considered statistically significant at a significance level of 90%.

3. RESULTS AND DISCUSSION

3.1 Apatite nanoparticles synthesis and characterization

3.1.1 Synthesis and characterization of AP-NPs. Nanocrystalline AP-NPs with physical-chemical features very close to biogenic AP in terms of chemical composition, morphology and surface properties, were prepared at room temperature by an acid-base neutralization reaction. This material exhibited XRD pattern characteristic of poorly crystalline AP single phase (Fig. 1A). Only AP peaks were detected, which can be indexed according to the crystallographic features of hydroxyapatite (hexagonal, space group P63/m, JCPDS file 09-432). The mean crystallite sizes (Table 1), calculated from the (310) and (002) planes applying the Scherrer's formula, evidenced that the NPs are elongated along the *c*-axis. TEM observations of AP revealed slightly elongated nano-platelets of about 30-50 nm (Fig. 1B), analogous to those found for bone mineral.[9] The Ca/P ratio was 1.70±0.03 close to the stoichiometric ratio of hydroxyapatite (Table 1).

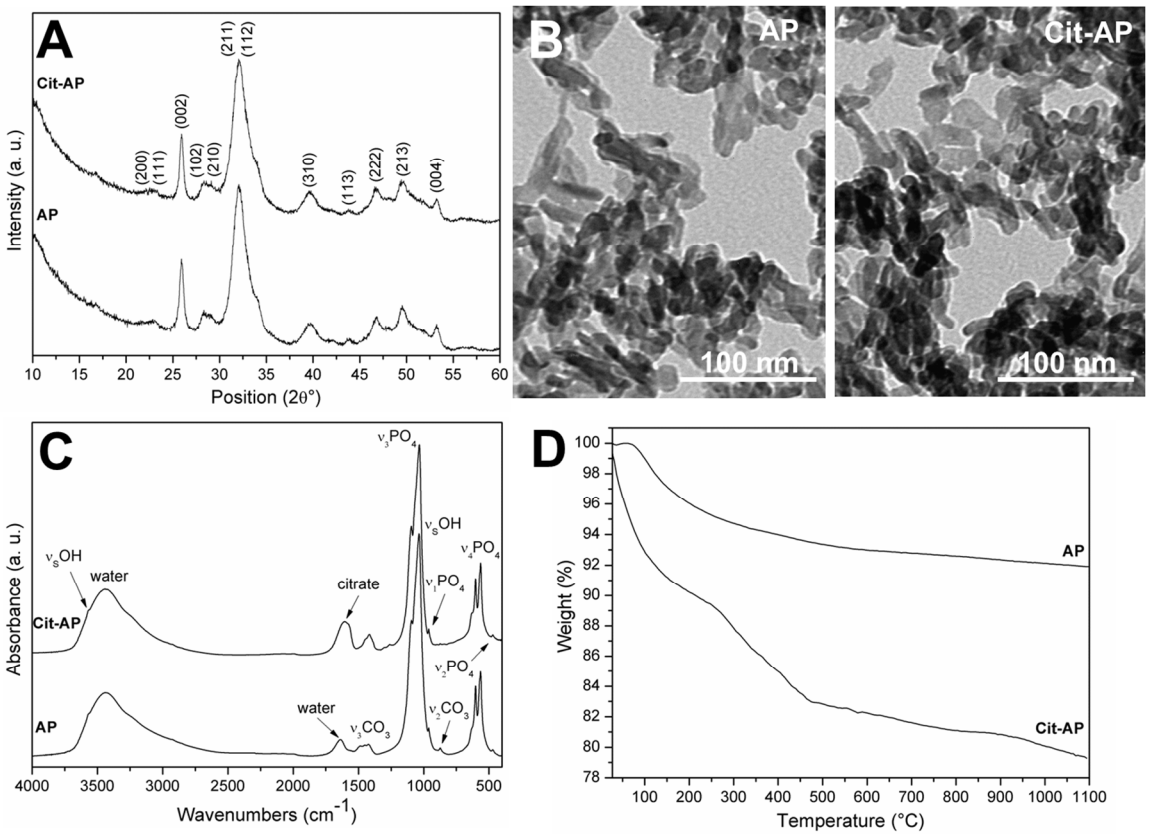

Figure 1. (A) XRD patterns, (B) TEM images, (C) FT-IR spectra and (D) TGA curves of AP and Cit-AP.

FTIR and Raman spectra of the AP (Fig. 1C and ESI Fig. S3, respectively) showed the characteristic vibration bands of AP, such as the apatitic PO_4^{3-} vibration bands at 470 (ν_2), 565−603 (ν_4), 962 (ν_1), and 1000−1104 cm^{-1} (ν_3).[38-39] Moreover, since the AP synthesis has not been carried out under inert gas, it exhibited FTIR bands at 870 (ν_2), 1420, and 1470 cm^{-1} (ν_3) assignable to CO_3^{2-} vibrations characteristic of B-type carbonate-apatite (*i.e.*, CO_3^{2-} replacing PO_4^{3-}).[38-39] These signals were consistent with the presence of a limited amount of carbonate derived from the atmospheric CO_2 adsorbed on the surface and/or entrapped in the lattice of the material. The vibration bands of OH^- at 3570 (νOH) and 632 cm^{-1} (ν_LOH, libration mode) were clearly distinguished in the Raman spectrum of AP (ESI Fig. S3, spectrum a). Additionally, a

small amount of acetate remained entrapped on the surface of AP as revealed by the presence of a weak Raman peak at *ca.* 2938 cm^{-1}, assignable to the $\nu_s CH_3$ of acetate ions.

Table 1. Bulk Ca/P, specific surface area (SSA_{BET}), mean crystallite sizes along the c- and ab-axis (D_{002} and D_{310}, respectively), ζ-potential, mean hydrodynamic radius (R_H) and polydispersity index (PDI) of AP and Cit-AP.

Sample	Ca/P[a]	SSA_{BET} (m^2g^{-1})[b]	D_{002} (nm)[c]	D_{310} (nm)[c]	ζ-potential (mV)[d]	R_H (nm)[e]	PDI
AP	1.70±0.03	160±10	22±4	7±3	-3.90±0.5	1514±189	0.42±0.03
Cit-AP	1.79±0.04	180±15	22±4	7±3	-33.2±0.4	140±2	0.17±0.01

[a]Determined by ICP-OES; [b]Determined by BET measurements; [c]Calculated by applying the Scherrer's equation; [d]Determined by electrophoretic mobility measurements in 0.01 M HEPES buffer at pH 7.0 and 25°C; [e]Determined by DLS (1 mg ml^{-1}) in 0.01 M HEPES buffer at pH 7.0 and 25°C.

One of the peculiar feature of synthetic biomimetic AP crystals is the existence of a hydrated surface layer with different composition and structure from the crystalline core, composed of water and rather labile ions (e.g. Ca^{2+}, HPO_4^{2-}, CO_3^{2-}) incorporated in the apatitic domains.[40] This layer is responsible for most of the properties of biomimetic AP, and in particular their high surface reactivity with surrounding biological fluids (which is directly linked to a high mobility of ionic species contained within this layer, as witnessed by fast surface ion exchange reactions).[40] FTIR is probably the most suitable analytical technique to evaluate the structural and physical-chemical properties of AP hydrated layer.[41] The curve-fitting analysis of the FTIR

spectra of AP in the ν_4PO_4 (700-500 cm^{-1}) and in the ν_3CO_3 (820-920 cm^{-1}) domains (ESI Fig. S2 and Table S1) evidenced the presence of non-apatitic phosphate signals at 610 cm^{-1} (PO_4^{3-}), 544 cm^{-1} (HPO_4^{2-}) and labile carbonate (856 cm^{-1}) on non-apatitic sites within the surface hydrated layer, as previously reported.[41]

All the above chemical analyses highlighted the biomimetic feature of AP-NPS, thanks to the evident morphological and structural similarities with the inorganic phase of bone.

3.1.2 Synthesis and characterization of Cit-AP-NPs. The major drawback in the use of NPs for nanomedical applications (especially in the case of calcium phosphates) is related to their fast tendency to form aggregates in aqueous suspension. In fact, the mean hydrodynamic radius (R_H) of AP-NPs (0.5 mg ml^{-1}) calculated by DLS was 1514±189 nm with a high polydispersity index (PDI) of 0.42±0.03 (Table 1). In the last years, to improve the colloidal stability of AP-NPs, their surface was modified with different molecules, such as L-lactic acid, poly(ε-caprolactone), ethylene glycol, polyethylenimine, glycosaminoglycans, poly(acrylic acid).[42-45] In this work, to avoid the use of synthetic compounds that may be potentially cytotoxic or cause allergic reactions as well as to preserve the biomimetic feature of the materials, a post-synthesis surface modification of AP with citrate, which is a simple and biocompatible molecule, was carried out putting in contact AP-NPs with an aqueous solution of citrate for 2 h. To remove unreacted citrate ions, dialysis was preferred because this procedure, differently from centrifugation or filtration, can avoid some irreversible agglomeration of adjacent particles during the purification step. The complete removal of the unreacted ions was assessed by measuring the conductivity of the dialysis medium (outside the membrane) as a function of time (ESI Fig. S4).

Citrate ions are biocompatible calcium complexing agents and growth inhibitors of AP.[46-47] Citrate is also present in bone where it accounts for about 5.5 wt% of the total organic component.[48] The strongly association of this molecule with the surface of biological bone AP was recently shown by NMR,[48] and further studies proposed that citrate is able to stabilize and to control size, thickness and morphology of AP crystals.[49-50] The concept of using citrate to form stable colloidal suspensions of hydroxyapatite NPs is not new per se,[47, 51-53] but in most of these studies, citrate has been added as active component during the synthesis.

The XRD pattern (Fig. 1A), the mean crystallite sizes calculated from the (002) and (310) planes and the SSA_{BET} (Table 1) of Cit-AP were analogous to those of AP. Similarly, previous works[53-54] detected any differences in XRD patterns and SSA_{BET} of hydroxyapatite NPs post-citration. In contrast to post-synthesis citration, the addition of citrate during the synthesis has important effect on crystal phase, particles size and crystallinity.[39, 50] TEM images of Cit-AP (Fig. 1B) displayed NPs very close to the AP-NPs, indicating that morphology and size were neither affected by the post-synthesis addition of citrate. On the other hand, ζ-potential and size distribution as well as mean R_H of Cit-AP were significantly different respect to AP (Table 1 and ESI Fig. S5). Surface modification with citrate provided the NPs with more negative surface potential (-33.2±0.4 mV), which in turn increased inter-particles repulsion. As result, Cit-AP-NPs were more de-aggregated forming a stable colloidal suspension with a mean R_H of 140±2 nm and a reduced PDI of 0.17±0.01 (Table 1). The colloidal stability of an aqueous suspension of Cit-AP-NPs or AP-NPs (0.5 mg ml^{-1}) as a function of time has been evaluated by DLS measuring continuously for 100 min the R_H as well as the mean count rate (ESI Fig. S6). In the case of Cit-AP-NPs, both values remained nearly constant corroborating that neither aggregation nor sedimentation occurred. The amount of citrate attached to the NPs was quantified by

comparing the TGA curves of AP and Cit-AP (Fig. 1D). TGA curve of Cit-AP, unlike that of AP, showed a substantial weight loss between 200 and 600 °C, that is the typical range of temperature where organic molecules are subject to thermal degradation. As a result, the percentages weight loss at 1100 °C of Cit-AP (21±2 wt%) was significantly higher than AP (9±1 wt%), revealing an amount of citrate attached to AP of about 12±2 wt%.

Several works focused on the adsorption of citrate on hydroxyapatite reported that this interaction occurred through an ion exchange of phosphate for citrate ions at the solid/liquid interface.[54-56] However, since hydroxyapatite NPs can be synthesized with several methods producing materials with different surface features, the ionic exchange cannot be seen as a general event and the interaction mechanism between citrate and hydroxyapatite still deserves investigation. To this aim, the amount of Ca^{2+} and PO_4^{3-} released from AP during citration (pH 9.3±0.2) and, as comparison, in ultrapure water (pH 8.0±0.2) has been quantified by ICP-OES (ESI Fig. S7). Results indicated a strong increase of the weight percentage of Ca^{2+} and PO_4^{3-} released from AP when citrate is present in the solution. This finding cannot be related to a pH-dependent dissolution because the pH values were similar and basic in both cases. In presence of citrate the released amount of PO_4^{3-} was higher than Ca^{2+}. The high amount of PO_4^{3-} released during citration can be consistent with a surface ionic exchange of citrate for PO_4^{3-} in line with the information previously reported.[54-56] Moreover, a structural rearrangement of the hydrate layer occurred, explaining also the significant removal of Ca^{2+} ions. The Ca/P of Cit-AP (Table 1) was 1.79±0.04, higher than that of AP, due to the higher quantity of PO_4^{3-} rather than Ca^{2+} released from AP. The Ca^{2+} and PO_4^{3-} contents for Cit-AP determined by ICP-OES were 31.67±0.59 and 41.92±0.53 wt%, respectively, lower than those for AP (Ca 34.82±0.59 wt% and PO_4^{3-} 48.57±0.17 wt%), in agreement with the presence of about the 12±2 wt% of citrate.

FTIR spectra of Cit-Ap (Fig. 1C) mainly showed the same phosphates signals of AP with the addition of the band at ca. 1600 cm^{-1} assignable to citrate ($\nu_{as}OCO$). Signals of citrate were also clearly distinguished at ca. 845 (ν CC), 1400-1600 ($\nu_{s}OCO$ and $\nu_{as}OCO$) and 2932 cm^{-1} (νCH_2) in the Raman spectrum of Cit-AP (ESI Fig. S3, spectrum b). The deconvolution of the ν_3CO_3, ν_2CO_3 and ν_4PO_4 FTIR signals of Cit-AP (ESI Fig. S2 and Table S1) indicated that also the carbonate content is clearly affected by the citration process. Indeed, a significant reduction of carbonate ions, mainly occupying B-positions (i.e., replacing phosphate ions), was observed after the functionalization with citrate. In addition, the detailed analysis of the ν_4PO_4 features enabled to distinguish that the non-apatitic environments[9] were slightly decreased after the citration process. Both findings confirmed that using our protocol, citrate ions were efficiently substituted for carbonate and phosphate ions of the surface hydrated layer of AP by ionic exchange. According to XRD, TEM, FTIR and Raman characterizations, we can also assume that citration process did not modify the core of the NPs but only their surface properties.

3.2 Labeling of apatite NPs with radiotracers

3.2.1 Radiolabeling efficiency and adsorption kinetics. AP-NPs and Cit-AP-NPs were radiolabeled with Fluorine-18 and Gallium-68 by simply mixing an aqueous solution of $[^{18}F]F^-$ or ^{68}Ga-NO2AP^{BP} with NPs suspensions. Adsorption kinetic studies (Fig. 2) established that the binding equilibrium of the two radiotracers towards AP and Cit-AP was promptly achieved (in less than 10 min). In fact, after 1 min of interaction followed by centrifugation, almost the total initial activity of the radiotracers (>93%) was already found in the pellet (AP) or in the filter (Cit-AP).

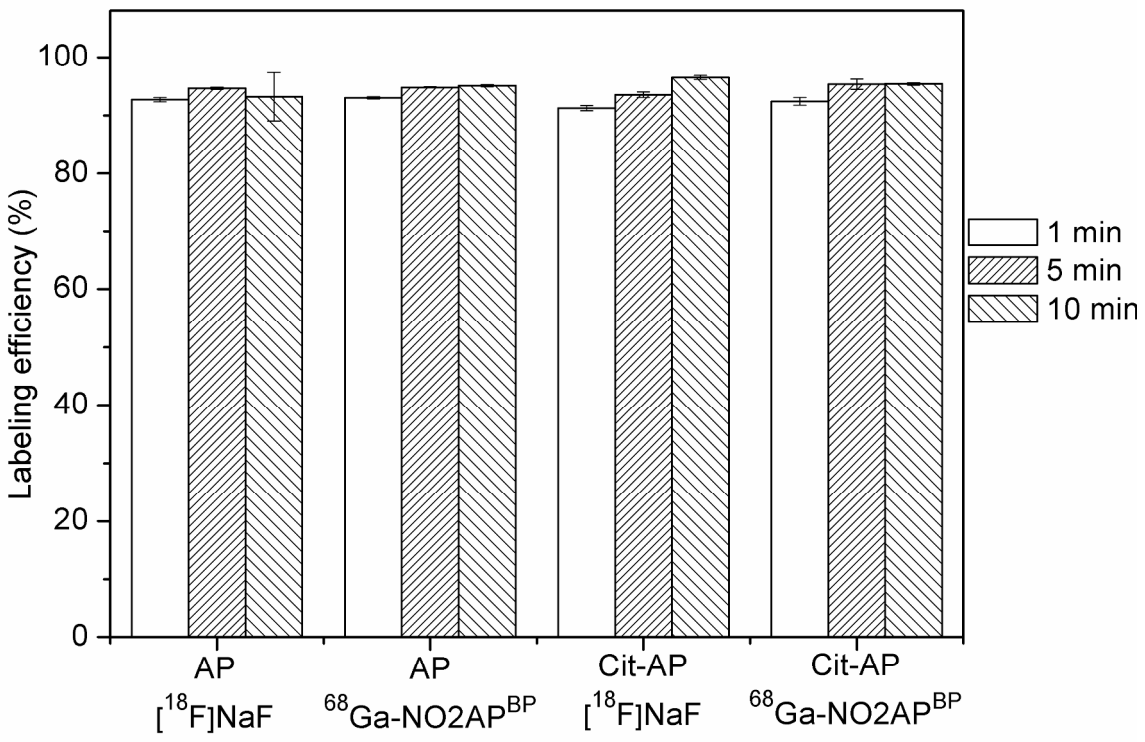

Figure 2. Adsorption kinetics of [^{18}F]NaF and ^{68}Ga-NO2AP^{BP} onto AP and Cit-AP

At each time point similar values were obtained comparing AP with Cit-AP and [^{18}F]NaF with ^{68}Ga-NO2AP^{BP}. These findings suggested that the uptake of the tracers is an instantaneous process, which cannot be analyzed with higher temporal resolution due to the period required for centrifugation.

To evaluate the specificity of the ^{68}Ga-NO2AP^{BP} interactions with AP and Cit-AP, adsorption kinetics of ^{68}Ga-NOTA and ionic $^{68}Ga^{3+}$ have been also carried out (ESI Fig. S8). While ^{68}Ga-NO2AP^{BP} with its bisphosphonate moiety was strongly attached to AP or Cit-AP, ^{68}Ga-NOTA, the analog macrocyclic chelator without phosphonate groups (ESI Fig. S1) showed neither affinity for AP nor for Cit-AP. Ionic $^{68}Ga^{3+}$ instead is also intensely attached to the NPs surface with the similar extent of ^{68}Ga-NO2AP^{BP} and [^{18}F]NaF. Process of cation exchange with Ca^{2+}

can explain the uptake of $^{68}Ga^{3+}$, as it was observed for other divalent and trivalent ions, such as Sn^{2+}, Zn^{2+}, Fe^{2+} and Al^{3+}, La^{3+}, Fe^{3+} respectively.[57-58] Because of the possible binding of ionic $^{68}Ga^{3+}$ with transferrins,[59-60] the labeling of the NPs with $^{68}Ga^{3+}$ assisted by chelating molecules with bisphosphonate arms was thought to be more effective for PET imaging. In fact, if the tracers are released from the NPs, they could be easily recognized since they might give a clear background image of the bone. As it is well known that basic pH values promote hydrolysis and precipitation of Ga^{3+},[61] the activity detected in the pellets could also indicate false positive adsorption of Ga^{3+} ions onto NPs. Therefore control experiments (without AP-NPs) were carried out showing any significant separation of activity and hence confirming the specific adsorption of $^{68}Ga^{3+}$ on the NPs.

3.2.2 Kinetic stability in different media. Kinetic stability studies of the radiolabeled NPs in isotonic saline solution and in PBS (Fig. 3) showed that AP and Cit-AP labeled with [^{18}F]NaF were stable in both media for a period up to 120 min (more than 95% of the radioactivity was found in the NPs). Thus, almost any significant desorption of the tracer can be expected *in vivo* in physiological conditions.

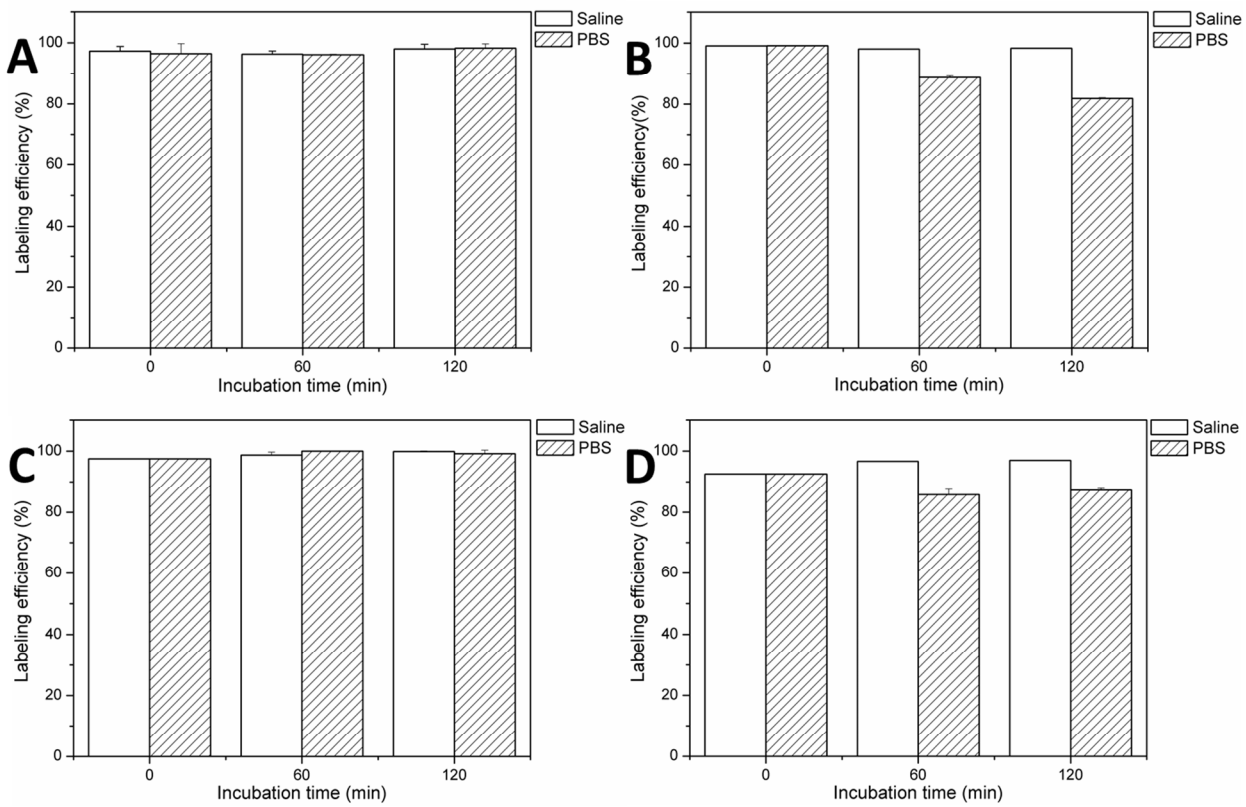

Figure 3. Kinetic stability in isotonic saline solution and PBS of AP-NPs labeled with (A) [^{18}F]NaF and (B) ^{68}Ga-NO2AP^{BP} and Cit-AP-NPs labeled with (C) [^{18}F]NaF and (D) ^{68}Ga-NO2AP^{BP}.

AP and Cit-AP labeled with ^{68}Ga-NO2AP^{BP} were also completely stable in saline for 120 min (more than 95% of the radioactivity was found in the NPs), while they resulted in minimal radiolabel loss in PBS over a period of 60 min. The activity loss was similar for AP and Cit-AP (about 15%). The low amount of ^{68}Ga-NO2AP^{BP} detached in PBS can be due to the presence of phosphate ions in the medium. The presence of phosphate species in solution triggered the release of bisphosphonates from AP-NPs and Cit-AP-NPs by ion-exchange as already well described in a previous work.[62]

These findings pointed out that both radiolabeling strategies should exhibit favorable stability properties *in vivo*.

3.2.3. Adsorption isotherms. The adsorbed amount of NaF and $NO2AP^{BP}$ (Q, μmol per mg of NPs) was plotted against their concentration in solution at equilibrium (Ce, mM) (Fig. 4). The isotherms clearly showed that the NPs exhibited high capacity of loading the corresponding tracers (higher than 0.1 μmol of tracer per mg of NPs). This fact enabled an effective radiolabeling of NPs in the range of 100 MBq to 1 GBq, considering the very low amounts of [^{18}F]NaF (pmol) and ^{68}Ga-$NO2AP^{BP}$ (nmol) used to label AP and Cit-AP with a radioactivity of about 100 MBq. The adsorption curves of $NO2AP^{BP}$ (Figs. 4 C,D) in comparison to those of NaF (Figs. 4 A,B) were characterized by a higher initial slope, indicating higher affinity for the NPs. As the concentration of the tracers increased in the solution, also the uptake increased, until completion.

The Langmuir,[63] Freundlich,[64] and Langmuir-Freundlich[65] models have been utilized to describe the adsorption isotherms (ESI Figs. S9 and S10). In all the cases the Langmuir-Freundlich model gave the best fit, which was confirmed by R^2 from linearized plots (ESI Fig. S9). The corresponding best fit-model curves and parameters (Q_{max}, K_{LF} and r), are reported in Fig. 4. The fact that all the adsorption isotherm curves fitted better according to the Langmuir-Freundlich model indicated that the adsorption sites on the apatite surface were energetically heterogeneous, due to the presence of the different chemical species (calcium, phosphates, citrate), as also confirmed by the fact that the calculated r coefficients were different to 1 (r=1, energetically homogeneous surface; r≠1, heterogeneous surface)[74] (Fig. 4). The constants K_{LF}, which provided a measure of the affinity of the tracer toward NPs, were significantly higher for

NO2AP^{BP} than NaF and in both cases they were higher for AP than Cit-AP. These data revealed that the presence of adsorbed citrate could be view as a sort of obstacle in the uptake of NO2AP^{BP} and NaF.

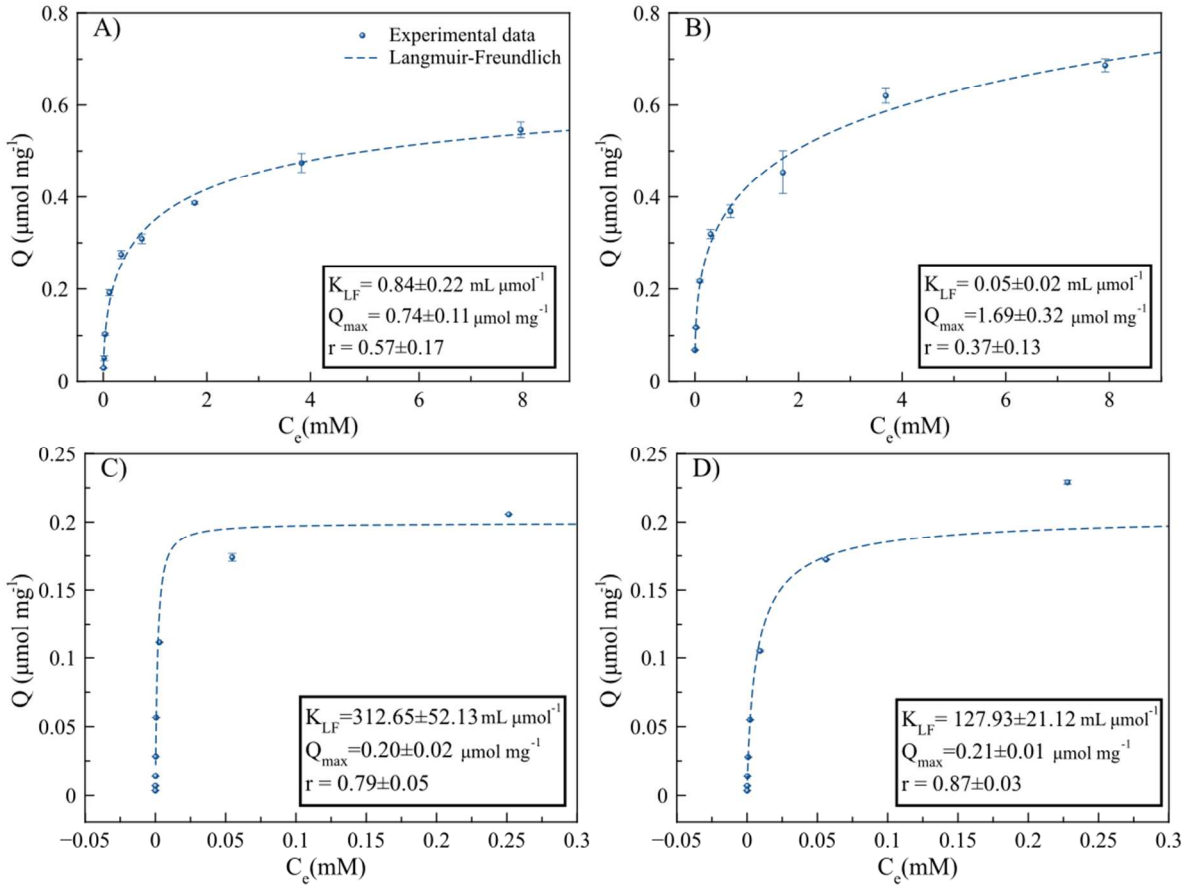

Figure 4. Adsorption isotherms of NaF on (A) AP and (B) Cit-AP and of NO2AP^{BP} on (C) AP and (D) Cit-AP. Separated points are the experimental data; dotted lines represent the non-lineal weighted least-squares (NWLS) fitting of the experimental data by using Langmuir–Freundlich (L-F) model. In each panel the corresponding best-fit adsorption parameters calculated according to L-F model are also reported.

The values of K_{LF} of NO2AP^{BP} on both NPs are in agreement with those reported by Rill et al.[66] who studied the adsorption of organic macrocyclic molecules with bisphosphonate side arm on hydroxyapatite. On the other hand, the theoretical maximum amount (Q_{max}) of NaF was higher for Cit-AP than AP, while this value was similar in the case of NO2AP^{BP} for Cit-AP and AP. This discrepancy can be due to different interaction mechanism of NaF and NO2AP^{BP} with NPs as well as the different size of the tracers.

3.3 Interaction mechanism of apatite NPs with radiotracers.

The interaction mechanisms of fluoride ions and bisphosphonates on hydroxyapatite NPs have been extensively investigated in the last years. Fluoride can interact with hydroxyapatite either by surface adsorption through ionic exchange or by substitution in the crystal lattice for hydroxyl group.[67] Bisphosphonates interaction with hydroxyapatite can be described as an ion exchange-reaction with the phosphates species on the apatitic surface and as a chemical binding of the phosphonates groups with the surface calcium sites of hydroxyapatite.[62] Nevertheless, the interactions between adsorbates and adsorbents strongly depend on the experimental conditions and the chemical-physical properties of the NPs.

In order to get more information on the interaction mechanism of [^{18}F]NaF and (B) ^{68}Ga-NO2AP^{BP} with AP and Cit-AP NPs and to evaluate how the labeling can affect the surface properties and the size of the NPs, AP and Cit-AP were functionalized with two different extents of "cold" NaF or NO2AP^{BP} and the mean R_H and the ζ-potential were measured (ESI Table S1). The functionalization of AP-NPs with low amount of NaF and NO2AP^{BP} affected neither the mean R_H nor the ζ-potential. Conversely, the coupling of AP-NPs with high amount of NaF and NO2AP^{BP} altered their surface charge. In particular the interaction with F^- caused a slightly shift

of the ζ-potential of AP toward values close to zero in agreement with an ion-exchange mechanism with OH^-. Differently, the functionalization with high amount of $NO2AP^{BP}$ altered significantly the ζ-potential of AP towards higher negative values due to the interaction of $NO2AP^{BP}$ with the surface calcium ions of AP and the resulting exposure of carboxylate moieties. The mean R_H of the AP-NPs functionalized with the highest amount of $NO2AP^{BP}$ was lower than that of the bare AP-NPs since the strong negative ζ-potential value decreased their tendency to form aggregates.

The mean R_H of Cit-AP was not substantially modified after the functionalization with F^- nor $NO2AP^{BP}$, while the ζ-potential values in both cases, and mainly when used higher amount of NaF and $NO2AP^{BP}$, shifted to higher positive values. These finding can be explained with a removal of citrate ions from the surface when Cit-AP interacted with $NO2AP^{BP}$ and with an ionic exchange of F^- for OH^- when interacted with NaF. It is important to underline that the amounts of NaF and $NO2AP^{BP}$ used for this latter characterization were much higher than those required to radiolabel the NPs, therefore we can assume that using both radiotracers the surface features and the size of labeled AP and Cit-AP were not significantly modified.

Raman spectra of AP and Cit-AP functionalized with the highest amount of NaF and $NO2AP^{BP}$ were collected (ESI Fig. S11), confirming that the interaction of the tracers with both NPs occurred mainly through ion-exchange mechanisms, as pointed out by DLS investigations. In fact, the intensity of the νOH Raman peak of AP and Cit-AP (3570 cm^{-1}) clearly was reduced after the functionalization with NaF (ESI Fig. S11 spectra b in panels A and B, respectively) suggesting in both cases an exchange of F^- for OH^-. Moreover, the νCC mode of citrate (845 cm^{-1}) of Cit-AP disappeared after the interaction with $NO2AP^{BP}$ (ESI Fig. S11, spectrum c in panel B), revealing ionic exchange between citrate and $NO2AP^{BP}$.

3.4 *In vivo* behavior of apatite NPs

The acquired observations regarding the radiolabeling efficiency, stability and mechanism of interaction of [^{18}F]NaF and ^{68}Ga-NO2AP^{BP} with AP and Cit-AP allowed the elucidation of a robust and fast method to label this kind of NPs, suitable for further *in vivo* investigations. Thus, AP-NPs and Cit-AP-NPs labeled with the selected tracers were injected intravenously into healthy Wistar rats and their behavior were tracked by dynamic PET imaging for 90 min. Fig. 5 depicts the coronal maximum intensity projections of the NPs 90 min after injection into the tail vein.

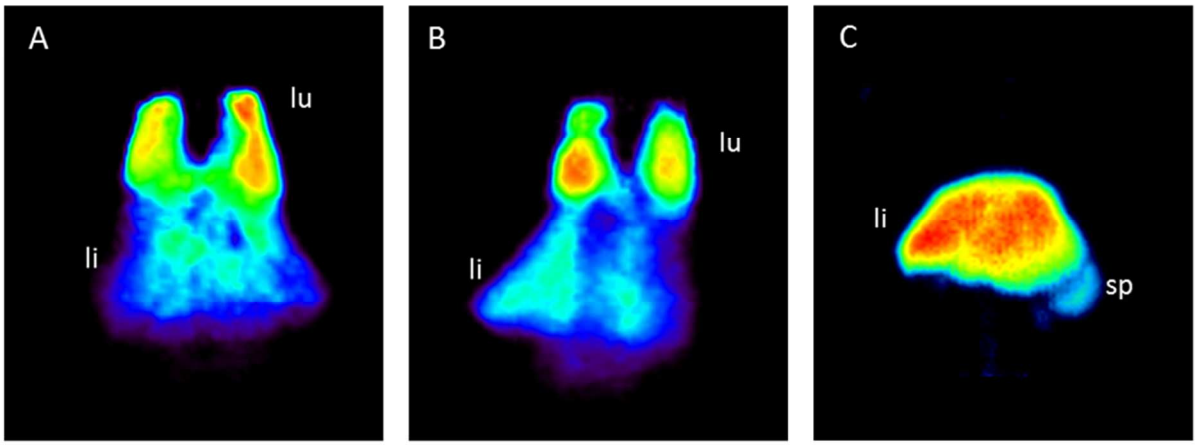

Figure 5. PET maximum intensity projections of the radiolabeled NPs in male healthy Wistar rats 90 min after injection. 0.1 mg of the NPs (15-22 MBq) was injected intravenously. Images represent the behavior of (A) [^{18}F]NaF-, (B) ^{68}Ga-NO2AP^{BP}-labeled AP-NPs and (C) ^{68}Ga-NO2AP^{BP}-labeled Cit-AP-NPs. (lu: lung, li: liver, sp: spleen).

It was clearly observable, that AP-NPs radiolabeled with [^{18}F]NaF or ^{68}Ga-NO2AP^{BP}, gave a strong PET signal *in vivo*. Both AP-NPs were almost completely entrapped by size exclusion in the lung which is the first physiological filter (Figs. 5A-B). This finding was explained by the fact that, as reported above, the AP-NPs which exhibited a severe tendency to form large aggregates (at the micrometric length scale), were not able to pass small vessels like the pulmonary capillary bed. Within 90 min, a low amount of radioactivity was revealed in the liver, since a few non-aggregated AP-NPs could be small enough to escape the first biological filtration mechanism or to be linked to serum proteins and further transported to the liver. It is important to remark that any uptake of the tracers in the joints of the skeleton (an area of typically enhanced bone growth and increased uptake of AP-targeting molecules) after 90 min was detected indicating that NPs entrapped in the lung capillary bed were stable towards loss of radiolabels. To better highlight the different behaviors of the free tracers versus those attached to AP-NPs, [^{18}F]NaF and [^{68}Ga]NO2AP^{BP} were injected in male healthy Wistar rats and visualized by PET (ESI Fig. S12). Images showed that differently from the activity revealed by labeled AP-NPs, a complete accumulation of the activity of both free tracers was detected in the bone and in the kidneys as previously reported.[32, 37]

Cit-AP radiolabeled with ^{68}Ga-NO2AP^{BP} gave also a strong PET signal *in vivo*, but contrary to AP-NPs, all of them were able to pass the lung within the first minutes and finally after 90 min accumulated almost exclusively in the second filter, the liver (Fig. 5C). Like small amount of non-aggregated AP were slowly transported into the liver within 90 min after injection, few Cit-AP-NPs presented the same fate but into the spleen (Fig. 5C) which is a well-discussed final destination of administered inorganic and organic NPs.[68-69] Also in this case any uptake of the tracers in the joints of the skeleton was detected after 90 min indicating high stability of the

^{68}Ga-NO2AP^{BP} labeled Cit-AP. In view of the similar *in vivo* behavior of ^{18}F- and ^{68}Ga-NO2AP^{BP}-labeled AP-NPs, the comparable physical-chemical properties of ^{18}F- and ^{68}Ga-NO2AP^{BP}-labeled Cit-AP-NPs and for ethical reasons, we decided to avoid the injection of ^{18}F-labeled Cit-AP-NPs in the rats. In fact, it was possible to hypothesize that also in the case of Cit-AP the fate of these NPs labeled with the two tracers were strongly analogous.

The presence of AP-NPs and Cit-AP-NPs in different organs was directly related to the higher tendency to form stable colloidal suspensions of Cit-AP rather than AP, which in turn have a strong impact in reducing the mean particle size. The accumulation of Cit-AP and small part of AP in the liver and spleen could potentially reflect phagocytosis of NPs by the reticuloendothelial system (RES). This system is known to phagocyte foreign materials of nanometric size and depending on the NPs characteristics (surface charge, hydrophobicity, shape, etc.) is one of the major causes of their removal from the blood.[70] The accumulation of AP and Cit-AP in organs of the RES (liver and spleen) and in the lung is completely in agreement with previous works that evaluated the biodistribution of intravenously administered hydroxyapatite NPs.[21, 23-24]

CONCLUSIONS

In this work the effective usage of citrate as biocompatible agent to strongly reduce aggregation and to stabilize hydrocolloids of biomimetic AP-NPs was fully demonstrated. The post-synthesis surface modification of AP with citrate occurred mainly by surface ionic exchange (citrate ions substituted for phosphate and carbonate ions) providing to the NPs a more negative surface potential, which in turn increased inter-particles repulsion.

Afterwards, naked AP-NPs and Cit-AP-NPs were efficiently radiolabeled with [^{18}F]NaF and ^{68}Ga-NO2AP^{BP}. In both cases the labeling was fast, facile, and straightforward, thus completely suitable for PET imaging. AP-NPs and Cit-AP-NPs have demonstrated excellent ability to bind significant quantities of both radiotracers and good *in vitro* stability in clinical relevant media. *In vivo* PET experiments in healthy Wistar revealed that [^{18}F]NaF and ^{68}Ga-NO2AP^{BP} labeled AP-NPs and Cit-AP-NPs gave strong PET signals and they were stable over the investigated time since any crucial tracer desorption was detected. These findings confirmed that the employments of both radiotracers are promising strategies for the future long term non-invasive monitoring of the biodistribution of structurally different AP-NPs by PET.

PET experiments have also allowed to track the fate of AP-NPs and Cit-AP-NPs *in vivo* in the first 90 min, indicating a clear ability of Cit-AP-NPs, unlike AP-NPs, to accumulate in different organs and to escape the first biological filters of lungs. This feature was directly related to the higher tendency to form stable colloidal suspensions of Cit-AP-NPs rather than AP-NPs.

In light of these results, and taking into account that AP-NPs can readily be further functionalized with targeting ligands, therapeutic agents and with metals for the combination of different imaging modalities, it can be concluded that apatite NPs are very promising materials in theranostic nanomedicine and they deserve further *in vitro* and *in vivo* studies.

ASSOCIATED CONTENT

Supporting Information. Sketch of NO2AP^{BP} and NOTA; Curve fitting of the FTIR spectra; Raman spectra; Conductivity evolution of dialysis medium as a function of time; Hydrodynamic radius and count rate as a function of time of NPs; Weight percentage of ions released from the NPs; Adsorption kinetics of ^{68}Ga-NOTA and $^{68}Ga^{3+}$ onto NPs; Fitting of adsorption isotherms;

PET images of free radiotracers. This material is available free of charge via the Internet at http://pubs.acs.org.

AUTHOR INFORMATION

Corresponding Author

*E-mail: frank.roesch@uni-mainz.de; michele.iafisco@istec.cnr.it

ACKNOWLEDGMENT

This research was supported by EU COST Action TD1004, "Theranostics Imaging and Therapy: an Action to Develop Novel Nanosized Systems for Imaging-Guided Drug Delivery", by the Italian Ministry for Education, University and Research (MIUR) in the framework of the Flagship Project NanoMAX (PNR 2011-2013) and by the grant of the Max Planck Graduate Center of the University of Mainz. JMDL activity was supported by the Spanish MINECO through the project Crysfunbio (MAT2011-28543) and the International Campus of Excellence (CEI-BioTic, University of Granada) through the project mP-BS-8.

REFERENCES

1. Sun, T.; Zhang, Y. S.; Pang, B.; Hyun, D. C.; Yang, M.; Xia, Y. Engineered Nanoparticles for Drug Delivery in Cancer Therapy. *Angew. Chem., Int. Ed.* **2014,** *53*, 12320-12364.
2. Pietronave, S.; Iafisco, M.; Locarno, D.; Rimondini, L.; Maria Prat, M. Functionalized Nanomaterials for Diagnosis and Therapy of Cancer. *J. Appl. Biomater. Biomech.* **2009,** *7*, 77-89.
3. Gao, J.; Xu, B. Applications of Nanomaterials Inside Cells. *Nano Today* **2009,** *4*, 37-51.
6. Iafisco, M.; Delgado-Lopez, J. M.; Varoni, E. M.; Tampieri, A.; Rimondini, L.; Gomez-Morales, J.; Prat, M. Cell Surface Receptor Targeted Biomimetic Apatite Nanocrystals for Cancer Therapy. *Small* **2013**, *9*, 3834-3844.
4. Wang, A. Z.; Langer, R.; Farokhzad, O. C. Nanoparticle Delivery of Cancer Drugs. *Annu. Rev. Med.* **2012,** *63*, 185-198.
5. Doane, T. L.; Burda, C. The Unique Role of Nanoparticles in Nanomedicine: Imaging, Drug Delivery and Therapy. *Chem. Soc. Rev.* **2012,** *41*, 2885-2911.

6. Iafisco, M.; Delgado-Lopez, J. M.; Varoni, E. M.; Tampieri, A.; Rimondini, L.; Gomez-Morales, J.; Prat, M. Cell Surface Receptor Targeted Biomimetic Apatite Nanocrystals for Cancer Therapy. *Small* **2013**, *9*, 3834-3844.
7. Hossain, S.; Yamamoto, H.; Chowdhury, E. H.; Wu, X.; Hirose, H.; Haque, A.; Doki, Y.; Mori, M.; Akaike, T. Fabrication and Intracellular Delivery of Doxorubicin/Carbonate Apatite Nanocomposites: Effect on Growth Retardation of Established Colon Tumor. *PLoS ONE* **2013,** *8*, e60428.
8. Al-Kattan, A.; Santran, V.; Dufour, P.; Dexpert-Ghys, J.; Drouet, C. Novel Contributions on Luminescent Apatite-Based Colloids Intended for Medical Imaging. *J. Biomater. Appl.* **2014**, *28*, 697-707.
9. Gómez-Morales, J.; Iafisco, M.; Delgado-López, J. M.; Sarda, S.; Drouet, C. Progress on the Preparation of Nanocrystalline Apatites and Surface Characterization: Overview of Fundamental and Applied Aspects. *Prog. Cryst. Growth Charact. Mater.* **2013,** *59*, 1-46.
10. Bose, S.; Tarafder, S., Calcium phosphate ceramic systems in growth factor and drug delivery for bone tissue engineering: A review. *Acta Biomater.* **2012,** *8* (4), 1401-1421.
11. Al-Kattan, A.; Girod-Fullana, S.; Charvillat, C.; Ternet-Fontebasso, H.; Dufour, P.; Dexpert-Ghys, J.; Santran, V.; Bordre, J.; Pipy, B.; Bernad, J.; Drouet, C. Biomimetic Nanocrystalline Apatites: Emerging Perspectives in Cancer Diagnosis and Treatment. *Int. J. Pharm.* **2012,** *423*, 26-36.
12. Iafisco, M.; Varoni, E.; Di Foggia, M.; Pietronave, S.; Fini, M.; Roveri, N.; Rimondini, L.; Prat, M. Conjugation of Hydroxyapatite Nanocrystals with Human Immunoglobulin G for Nanomedical Applications. *Colloids Surf., B* **2012,** *90*, 1-7.
13. Xie, G.; Sun, J.; Zhong, G.; Liu, C.; Wei, J. Hydroxyapatite Nanoparticles as a Controlled-Release Carrier of BMP-2: Absorption and Release Kinetics In Vitro. *J. Mater. Sci: Mater. Med.* **2010,** *21*, 1875-1880.
14. Cheng, X.; Kuhn, L. Chemotherapy Drug Delivery from Calcium Phosphate Nanoparticles. *Int. J. Nanomed.* **2007,** *2* (4), 667-674.
15. Chowdhury, E. H. pH-Sensitive Nano-Crystals of Carbonate Apatite for Smart and Cell-Specific Transgene Delivery. *Expert Opin. Drug Delivery* **2007,** *4*, 193-196.
16. Uskoković, V.; Uskoković, D. P. Nanosized Hydroxyapatite and Other Calcium Phosphates: Chemistry of Formation and Application as Drug and Gene Delivery Agents. *J. Biomed. Mater. Res., Part B* **2011,** *96B*, 152-191.
17. Chen, L.; Mccrate, J. M.; Lee, J. C.-M.; Li, H. The Role of Surface Charge on the Uptake and Biocompatibility of Hydroxyapatite Nanoparticles with Osteoblast Cells. *Nanotechnology* **2011,** *22*, 105708.
18. Turkez, H.; Yousef, M. I.; Sönmez, E.; Togar, B.; Bakan, F.; Sozio, P.; Stefano, A. D. Evaluation of Cytotoxic, Oxidative Stress and Genotoxic Responses of Hydroxyapatite Nanoparticles on Human Blood Cells. *J. Appl. Toxicol.* **2014,** *34*, 373-379.
19. Zhao, X.; Ng, S.; Heng, B.; Guo, J.; Ma, L.; Tan, T.; Ng, K.; Loo, S. Cytotoxicity of Hydroxyapatite Nanoparticles is Shape and Cell Dependent. *Arch. Toxicol.* **2013,** *87*, 1037-1052.
20. Zhao, X.; Ong, K. J.; Ede, J. D.; Stafford, J. L.; Ng, K. W.; Goss, G. G.; Loo, S. C. J. Evaluating the Toxicity of Hydroxyapatite Nanoparticles in Catfish Cells and Zebrafish Embryos. *Small* **2013,** *9*, 1734-1741.
21. Jauregui-Osoro, M.; Williamson, P. A.; Glaria, A.; Sunassee, K.; Charoenphun, P.; Green, M. A.; Mullen, G. E. D.; Blower, P. J. Biocompatible Inorganic Nanoparticles for [18F]-Fluoride Binding with Applications in PET Imaging. *Dalton Trans.* **2011,** *40*, 6226-6237.

22. Ong, H.; Loo, J. C.; Boey, F. C.; Russell, S.; Ma, J.; Peng, K.-W. Exploiting the High-Affinity Phosphonate–Hydroxyapatite Nanoparticle Interaction for Delivery of Radiation and Drugs. *J. Nanopart. Res.* **2008,** *10*, 141-150.
23. Liu, Y.; Sun, Y.; Cao, C.; Yang, Y.; Wu, Y.; Ju, D.; Li, F. Long-Term Biodistribution In Vivo and Toxicity of Radioactive/Magnetic Hydroxyapatite Nanorods. *Biomaterials* **2014,** *35*, 3348-3355.
24. Ignjatović, N.; Vranješ Djurić, S.; Mitić, Ž.; Janković, D.; Uskoković, D. Investigating an Organ-Targeting Platform Based on Hydroxyapatite Nanoparticles Using a Novel in Situ Method of Radioactive 125Iodine Labeling. *Mater. Sci. Eng., C* **2014,** *43*, 439-446.
25. Stockhofe, K.; Postema, J. M.; Schieferstein, H.; Ross, T. L. Radiolabeling of Nanoparticles and Polymers for PET Imaging. *Pharmaceuticals* **2014,** *7*, 392-418.
26. Loudos, G.; Kagadis, G. C.; Psimadas, D. Current Status and Future Perspectives of In Vivo Small Animal Imaging Using Radiolabeled Nanoparticles. *Eur. J. Radiol.* **2011,** *78* 287-295.
27. Ting, G.; Chang, C. H.; Wang, H. E. Cancer Nanotargeted Radiopharmaceuticals for Tumor Imaging and Therapy. *Anticancer Res.* **2009,** *29*, 4107-4118.
28. Lee, D.-E.; Koo, H.; Sun, I.-C.; Ryu, J. H.; Kim, K.; Kwon, I. C. Multifunctional Nanoparticles for Multimodal Imaging and Theragnosis. *Chem. Soc. Rev.* **2012,** *41*, 2656-2672.
29. Welch, M. J.; Hawker, C. J.; Wooley, K. L. The Advantages of Nanoparticles for PET. *J. Nucl. Med.* **2009,** *50*, 1743-1746.
30. Sun, X.; Cai, W.; Chen, X. Positron Emission Tomography Imaging Using Radiolabeled Inorganic Nanomaterials. *Acc. Chem. Res.* **2015,** *48*, 286-294.
31. Xing, Y.; Zhao, J.; Conti, P. S.; Chen, K. Radiolabeled Nanoparticles for Multimodality Tumor Imaging. *Theranostics* **2014,** *4*, 290-306.
32. Czernin, J.; Satyamurthy, N.; Schiepers, C. Molecular Mechanisms of Bone 18F-NaF Deposition. *J. Nucl. Med.* **2010,** *51*, 1826-1829.
33. Le Bars, D., Fluorine-18 and medical imaging: Radiopharmaceuticals for Positron Emission Tomography. *J. Fluorine Chem.* **2006,** *127*, 1488-1493.
34. Holub, J.; Meckel, M.; Kubíček, V.; Rösch, F.; Hermann, P. Gallium(III) Complexes of NOTA-bis (phosphonate) Conjugates as PET Radiotracers for Bone Imaging. *Contrast Media Mol. Imaging* **2015**, *10*, 122-134
35. Patterson, A. L. The Scherrer Formula for X-Ray Particle Size Determination. *Phys. Rev.* **1939,** *56*, 978-982.
36. Zhernosekov, K. P.; Filosofov, D. V.; Baum, R. P.; Aschoff, P.; Bihl, H.; Razbash, A. A.; Jahn, M.; Jennewein, M.; Rösch, F. Processing of Generator-Produced 68Ga for Medical Application. *J. Nucl. Med.* **2007,** *48*, 1741-1748.
37. Fellner, M.; Riss, P.; Loktionova, N.; Zhernosekov, K.; Thews, O.; Geraldes, C. F. G. C.; Kovacs, Z.; Lukeš, I.; Rösch, F. Comparison of Different Phosphorus-Containing Ligands Complexing 68Ga for PET-Imaging of Bone Metabolism. *Radiochim. Acta* **2011,** *99*, 43-51.
38. Koutsopoulos, S. Synthesis and Characterization of Hydroxyapatite Crystals: a Review Study on the Analytical Methods. *J. Biomed. Mater. Res., Part A* **2002,** *62*, 600-12.
39. Delgado-López, J. M.; Iafisco, M.; Rodríguez, I.; Tampieri, A.; Prat, M.; Gómez-Morales, J. Crystallization of Bioinspired Citrate-Functionalized Nanoapatite with Tailored Carbonate Content. *Acta Biomater.* **2012,** *8*, 3491-3499.

40. Rey, C.; Combes, C.; Drouet, C.; Cazalbou, S.; Grossin, D.; Brouillet, F.; Sarda, S. Surface Properties of Biomimetic Nanocrystalline Apatites; Applications in Biomaterials. *Prog. Cryst. Growth Charact. Mater.* **2014,** *60*, 63-73.
41. Drouet, C.; Carayon, M. T.; Combes, C.; Rey, C. Surface Enrichment of Biomimetic Apatites with Biologically-Active Ions Mg2+ and Sr2+: A Preamble to the Activation of Bone Repair Materials. *Mater. Sci. Eng., C* **2008,** *28*, 1544-1550.
42. Lee, H. J.; Choi, H. W.; Kim, K. J.; Lee, S. C. Modification of Hydroxyapatite Nanosurfaces for Enhanced Colloidal Stability and Improved Interfacial Adhesion in Nanocomposites. *Chem. Mater.* **2006,** *18*, 5111-5118.
43. Ashokan, A.; Menon, D.; Nair, S.; Koyakutty, M. A Molecular Receptor Targeted, Hydroxyapatite Nanocrystal Based Multi-Modal Contrast Agent. *Biomaterials* **2010,** *31* (9), 2606-2616.
44. Han, Y.; Wang, X.; Li, S. A Simple Route to Prepare Stable Hydroxyapatite Nanoparticles Suspension. *J. Nanopart. Res.* **2009,** *11*, 1235-1240.
45. Liou, S.-C.; Chen, S.-Y.; Liu, D.-M. Manipulation of Nanoneedle and Nanosphere Apatite/Poly(acrylic acid) Nanocomposites. *J. Biomed. Mater. Res., Part B* **2005,** *73B*, 117-122.
46. Lopez-Macipe, A.; Gomez-Morales, J.; Rodriguez-Clemente, R. Nanosized Hydroxyapatite Precipitation From Homogeneous Calcium/Citrate/Phosphate Solutions Using Microwave and Conventional Heating. *Adv. Mater.* **1998,** *10*, 49-53.
47. Li, C.; Zhao, L.; Han, J.; Wang, R.; Xiong, C.; Xie, X. Synthesis of Citrate-Stabilized Hydrocolloids of Hydroxyapatite through a Novel Two-stage Method: A Possible Aggregates–Breakdown Mechanism of Colloid Formation. *J. Colloid Interface Sci.* **2011,** *360*, 341-349.
48. Hu, Y.-Y.; Rawal, A.; Schmidt-Rohr, K. Strongly Bound Citrate Stabilizes the Apatite Nanocrystals in Bone. *Proc. Natl. Acad. Sci. U. S. A.* **2010**, *107*, 22425-22429.
49. Xie, B.; Nancollas, G. H. How to Control the Size and Morphology of Apatite Nanocrystals in Bone. *Proc. Natl. Acad. Sci. U. S. A.* **2010,** *107*, 22369-22370.
50. Iafisco, M.; Ramirez-Rodriguez, G. B.; Sakhno, Y.; Tampieri, A.; Martra, G.; Gomez-Morales, J.; Delgado-Lopez, J. M. The Growth Mechanism of Apatite Nanocrystals Assisted by Citrate: Relevance to Bone Biomineralization. *CrystEngComm* **2015,** *17*, 507-511.
51. Jin, X.; Zhuang, J.; Zhang, Z.; Guo, H.; Tan, J. Hydrothermal Synthesis of Hydroxyapatite Nanorods in the Presence of Sodium Citrate and its Aqueous Colloidal Stability Evaluation in Neutral pH. *J. Colloid Interface Sci.* **2015,** *443*, 125-130.
52. Leeuwenburgh, S. C. G.; Ana, I. D.; Jansen, J. A. Sodium Citrate as an Effective Dispersant for the Synthesis of Inorganic–Organic Composites with a Nanodispersed Mineral Phase. *Acta Biomater.* **2010,** *6*, 836-844.
53. Müller, K. H.; Motskin, M.; Philpott, A. J.; Routh, A. F.; Shanahan, C. M.; Duer, M. J.; Skepper, J. N. The Effect of Particle Agglomeration on the Formation of a Surface-Connected Compartment Induced by Hydroxyapatite Nanoparticles in Human Monocyte-Derived Macrophages. *Biomaterials* **2014,** *35*, 1074-1088.
54. López-Macipe, A.; Gómez-Morales, J.; Rodriguez-Clemente, R. The Role of pH in the Adsorption of Citrate Ions on Hydroxyapatite. *J. Colloid Interface Sci.* **1998,** *200*, 114-120.
55. Misra, D. N. Interaction of Some Alkali Metal Citrates with Hydroxyapatite: Ion-Exchange Adsorption and Role of Charge Balance. *Colloids Surf., A* **1998,** *141*, 173-179.
56. Skwarek, E.; Janusz, W.; Sternik, D. Adsorption of Citrate Ions on Hydroxyapatite Synthetized by Various Methods. *J. Radioanal. Nucl. Chem.* **2014,** *299*, 2027-2036.

57. Tanizawa, Y.; Sawamura, K.; Suzuki, T. Reaction Characteristics of Dental and Synthetic Apatites with Al3+ and La3+ Ions in Acidic Solutions. *J. Chem. Soc., Faraday Trans.* **1990,** *86*, 4025-4029.
58. Wakamura, M.; Kandori, K.; Ishikawa, T. Surface Structure and Composition of Calcium Hydroxyapatites Substituted with Al(III), La(III) and Fe(III) Ions. *Colloids Surf., A* **2000,** *164*, 297-305.
59. Fani, M.; André, J. P.; Maecke, H. R. 68Ga-PET: a Powerful Generator-Based Alternative to Cyclotron-Based PET Radiopharmaceuticals. *Contrast Media Mol. Imaging* **2008,** *3*, 53-63.
60. Brunetti, A.; Blasberg, R. G.; Finn, R. D.; Larson, S. M. Gallium-Transferrin as a Macromolecular Tracer of Vascular Permeability. *Nucl. Med. Biol.* **1988,** *15*, 665-672.
61. Green, M. A.; Welch, M. J. Gallium Radiopharmaceutical Chemistry. *Int. J. Radiat. Appl. Instrum., Part B* **1989,** *16*, 435-448.
62. Pascaud, P.; Errassifi, F.; Brouillet, F.; Sarda, S.; Barroug, A.; Legrouri, A.; Rey, C. Adsorption on Apatitic Calcium Phosphates for Drug Delivery: Interaction with Bisphosphonate Molecules. *J. Mater. Sci: Mater. Med.* **2014,** *25*, 2373-2381.
63. Langmuir, I. The Adsorption of Gases on Plane Surfaces of Glass, Mica and Platinum. *J. Am. Chem. Soc.* **1918,** *40*, 1361-1403.
64. Jaroniec, M. Adsorption on Heterogeneous Surfaces: The Exponential Equation for the Overall Adsorption Isotherm. *Surf. Sci.* **1975,** *50*, 553-564.
65. Sips, R. On the Structure of a Catalyst Surface. *J. Chem. Phys.* **1948,** *16*, 490-495.
66. Rill, C.; Kolar, Z. I.; Kickelbick, G.; Wolterbeek, H. T.; Peters, J. A. Kinetics and Thermodynamics of Adsorption on Hydroxyapatite of the [160Tb]Terbium Complexes of the Bone-Targeting Ligands DOTP and BPPED. *Langmuir* **2009,** *25*, 2294-2301.
67. Sternitzke, V.; Kaegi, R.; Audinot, J.-N.; Lewin, E.; Hering, J. G.; Johnson, C. A. Uptake of Fluoride from Aqueous Solution on Nano-Sized Hydroxyapatite: Examination of a Fluoridated Surface Layer. *Environ. Sci. Technol.* **2012,** *46*, 802-809.
68. Demoy, M.; Andreux, J.-P.; Weingarten, C.; Gouritin, B.; Guilloux, V.; Couvreur, P. Spleen Capture of Nanoparticles: Influence of Animal Species and Surface Characteristics. *Pharm. Res.* **1999,** *16*, 37-41.
69. Rojas, S.; Gispert, J. D.; Abad, S.; Buaki-Sogo, M.; Victor, V. M.; Garcia, H.; Herance, J. R. In Vivo Biodistribution of Amino-Functionalized Ceria Nanoparticles in Rats Using Positron Emission Tomography. *Mol. Pharmaceut.* **2012,** *9*, 3543-3550.
70. Nie, S. Understanding and Overcoming Major Barriers in Cancer Nanomedicine. *Nanomedicine (London, U. K.)* **2010,** *5*, 523-528.

Table of Contents/Abstract Graphic

The radiolabelling of apatite nanoparticles (naked and surface-modified with citrate to reduce aggregation) with two PET imaging agents ([^{18}F]NaF and ^{68}Ga-NO2AP^{BP}) was investigated. Using both tracers the labeling resulted fast and straightforward. *In vivo* PET experiments revealed a clear effect of citrated versus non-citrated nanoparticles to accumulate in different organs

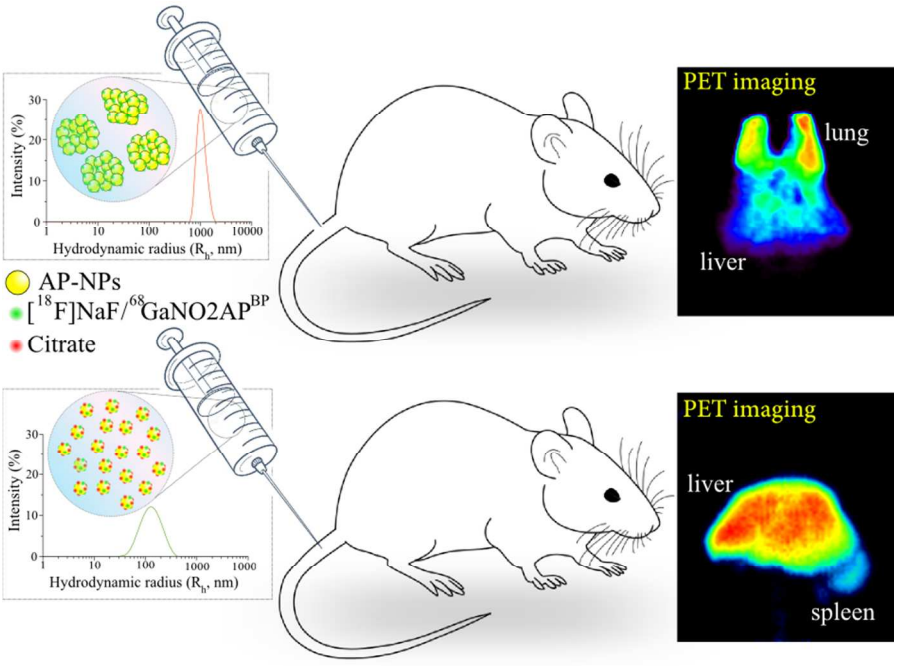

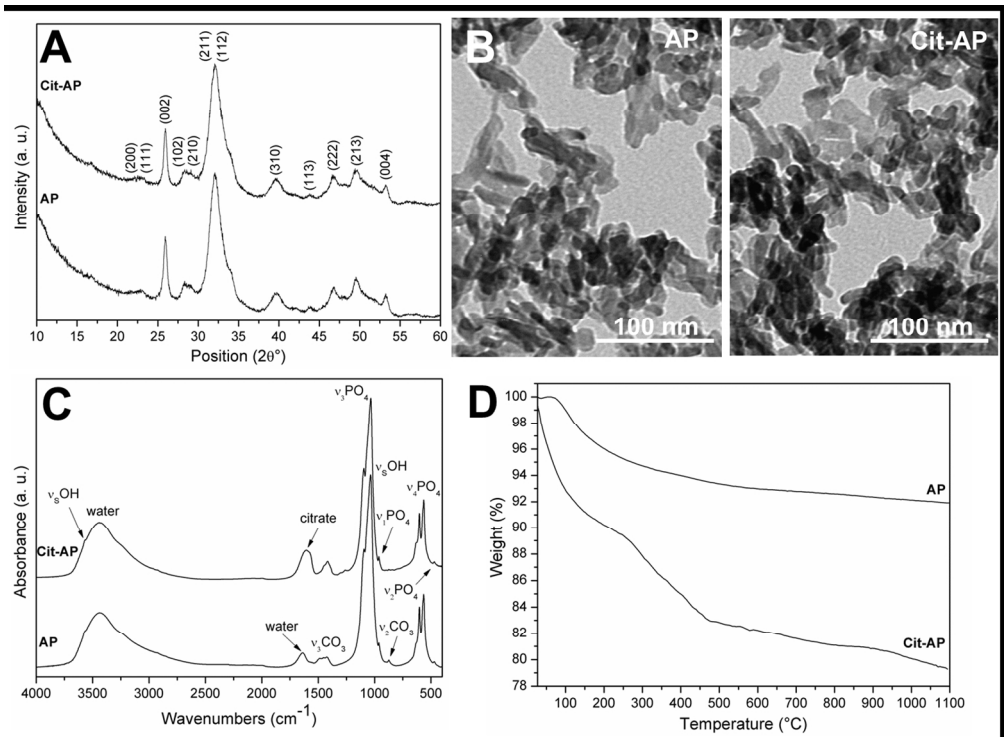

254x186mm (150 x 150 DPI)

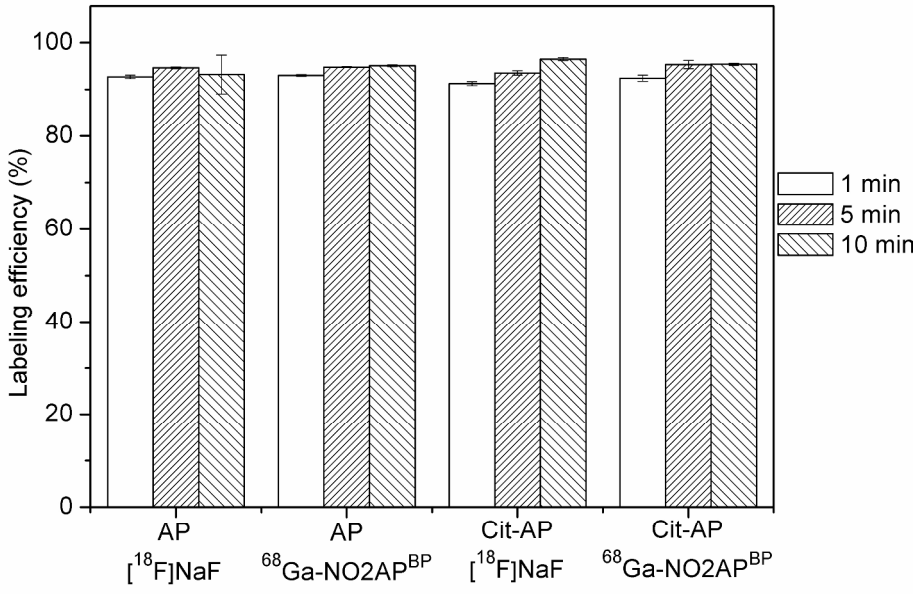

289x202mm (300 x 300 DPI)

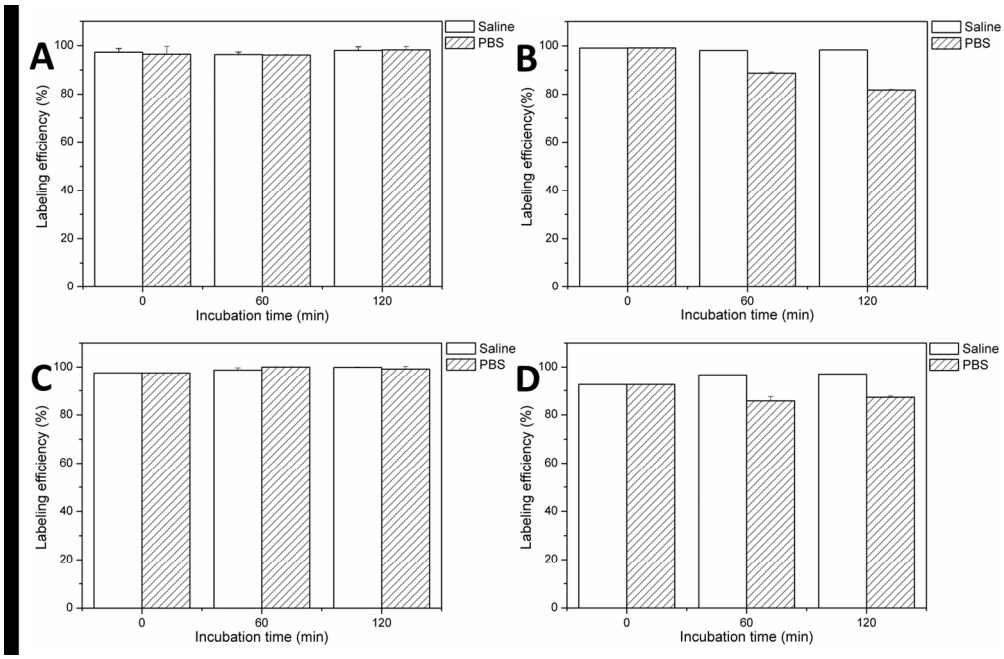

271x175mm (150 x 150 DPI)

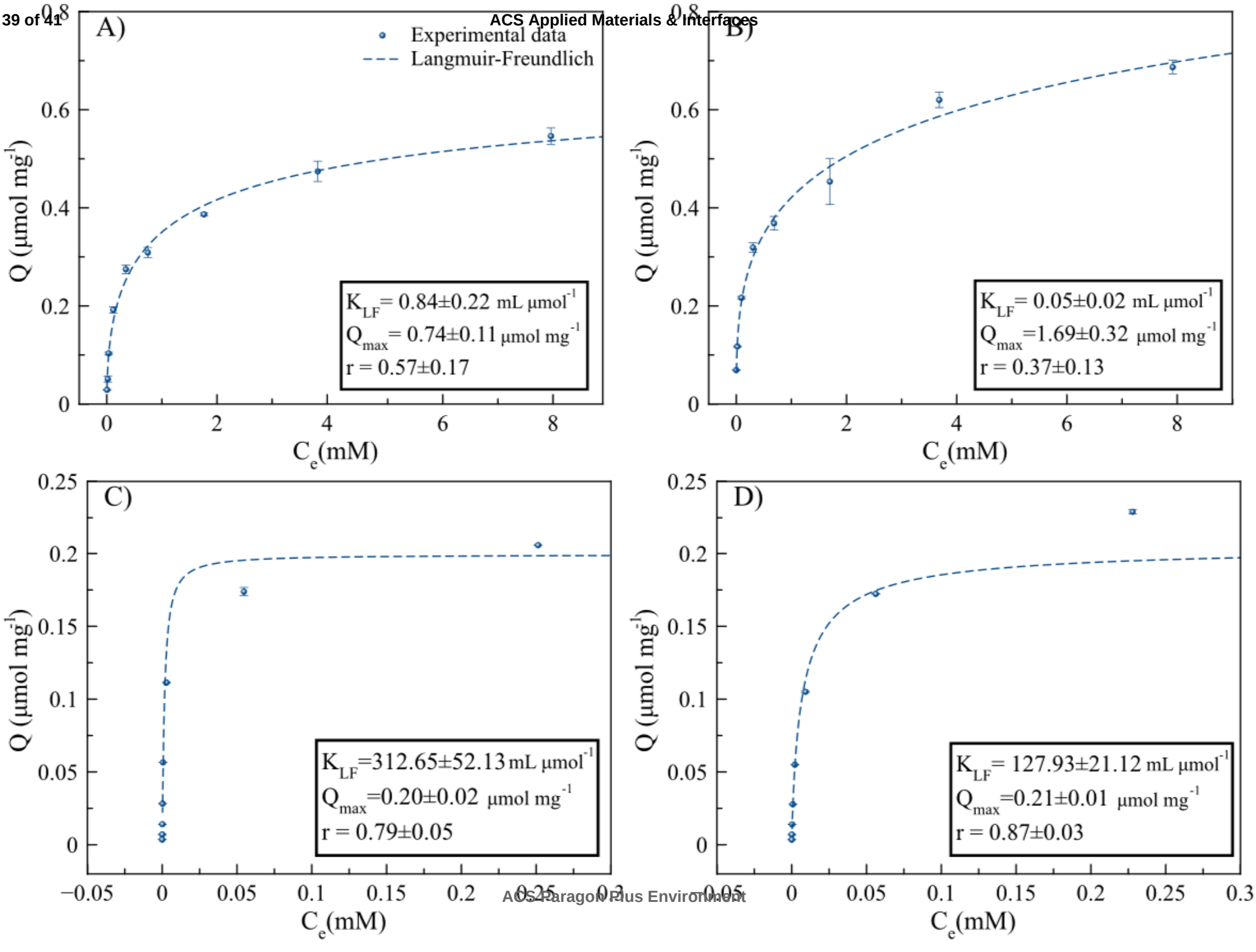
A)
Experimental data
Langmuir-Freundlich
K_{LF}= 0.84±0.22 mL μmol^{-1}
Q_{max}= 0.74±0.11 μmol mg^{-1}
r = 0.57±0.17
B)
K_{LF}= 0.05±0.02 mL μmol^{-1}
Q_{max}=1.69±0.32 μmol mg^{-1}
r = 0.37±0.13
C)
K_{LF}=312.65±52.13 mL μmol^{-1}
Q_{max}=0.20±0.02 μmol mg^{-1}
r = 0.79±0.05
D)
K_{LF}= 127.93±21.12 mL μmol^{-1}
Q_{max}=0.21±0.01 μmol mg^{-1}
r = 0.87±0.03
Q (μmol mg^{-1})
C_e(mM)

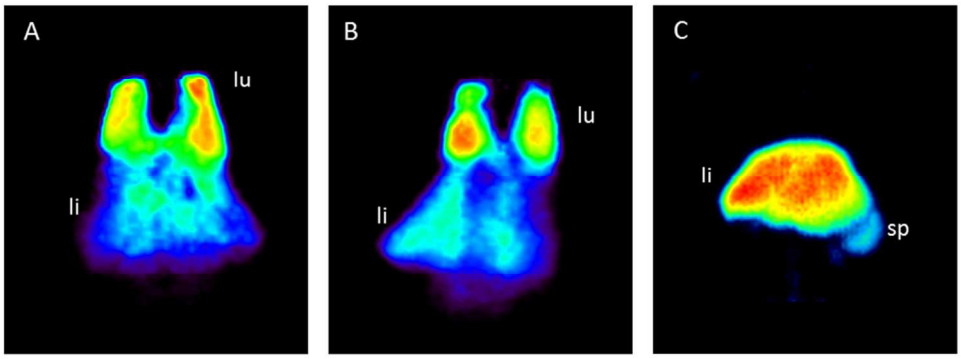

174x68mm (150 x 150 DPI)

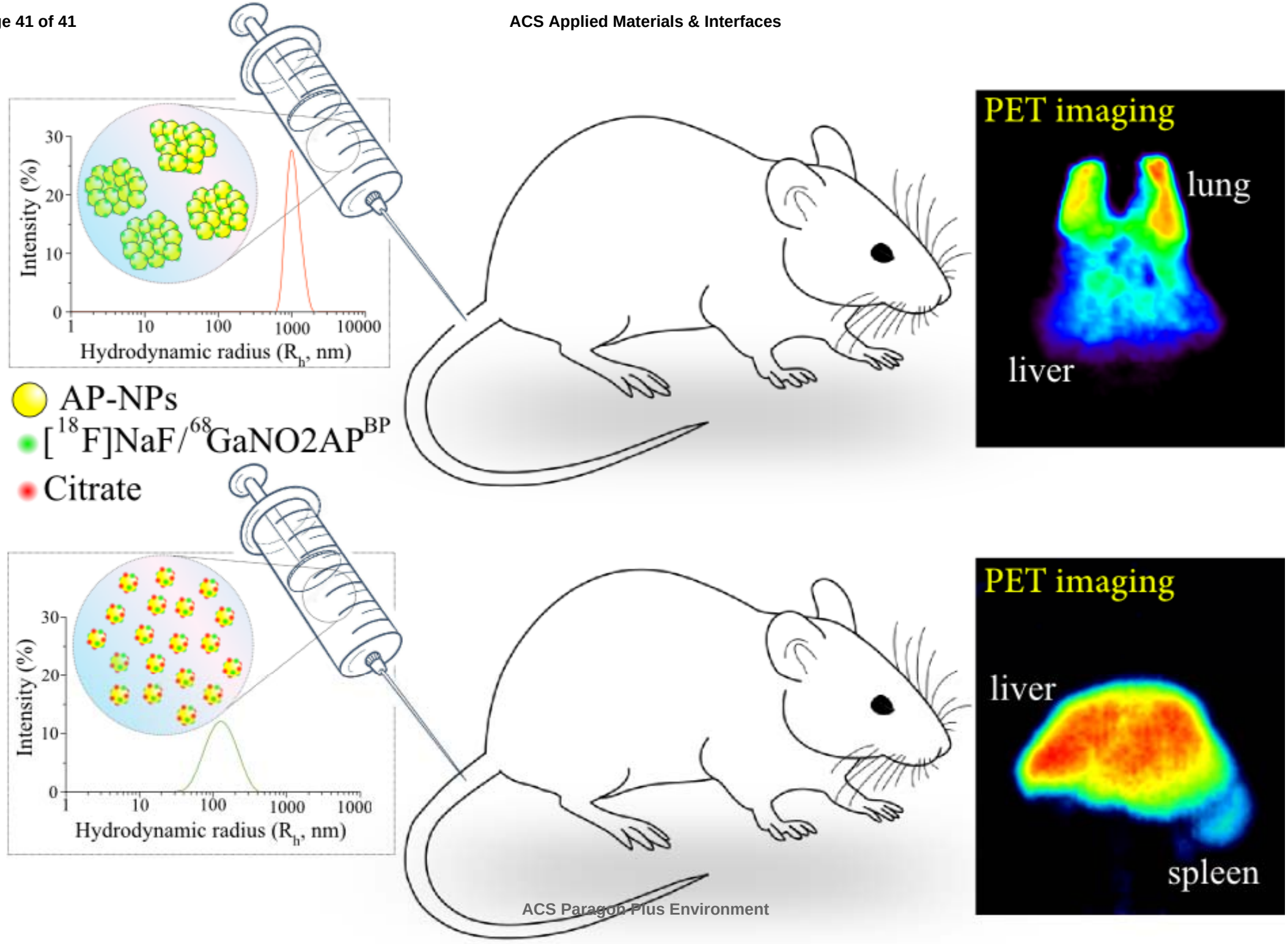
Intensity (%)
Hydrodynamic radius (R$_h$, nm)
AP-NPs
[^{18}F]NaF/^{68}GaNO2AP^{BP}
Citrate
PET imaging
lung
liver
PET imaging
liver
spleen